45th AIAA Aerospace Sciences Meeting and Exhibit
8 - 11 January 2007, Reno, Nevada

AIAA 2007-256

Results from the 3rd Drag Prediction Workshop Using the NSU3D Unstructured Mesh Solver

Dimitri J. Mavriplis *

Department of Mechanical Engineering, University of Wyoming, Laramie WY 82071, USA

Results from the third AIAA Drag Prediction Workshop using the unstructured mesh Reynolds averaged Navier-Stokes (RANS) solver NSU3D are presented. Computations include a grid convergence study on a transonic wing-body and wing-body-fairing configuration at a fixed C_L condition using grids up to 41 million points, as well as an incidence sweep (drag polar) at fixed Mach and Reynolds number. A second set of results on a pair of closely related wing geometries is also described, including a grid convergence study at fixed incidence, and an incidence sweep (drag polar) for both wing geometries. For all cases, approximate second-order accurate grid convergence characteristics are demonstrated, with overall accuracy and efficiency comparable to other structured, overset, and unstructured workshop calculations. However, it is found that differing grid converged results may be inferred based on different families of self-similar coarse and fine grid sequences, particularly for values such as absolute drag at fixed incidence. More consistent grid convergence for idealized drag values (omitting induced drag) is observed, thus validating the procedure of performing grid convergence studies at fixed C_L. These grid convergence issues are attributed to the large range of disparate scales which must be resolved in aerodynamic flows, and point to the need for further advances in quantifying and resolving discretization errors for such problems.

Over the last five years, the AIAA Applied Aerodynamics Committee has sponsored three Drag Prediction Workshops (DPW), with the aim of assessing the state-of-the-art of current Computational Fluid Dynamics (CFD) solvers at predicting absolute and incremental drag changes on generic transonic transport aircraft configurations.

The first workshop, DPW I, held in Anaheim CA, in June 2001, employed the DLR-F4 wing-body geometry[1,2] due to its simplicity and relevance to modern transonic transport aircraft design studies, as well as due to the availability of publicly released experimental data. The second workshop, DPW II, held in Orlando FL, in June 2003, employed the slightly different DLR-F6 geometry, which included a wing-body configuration, and a wing-body-nacelle-pylon configuration, both of which have been tested experimentally. DPW II thus offered the possibility to study increments in drag between two similar configurations, as would be typically done in a design study. In both workshops, test cases were devised to mimic industrial design practices, and these included fixed C_L single-point solutions, drag polars, and fixed C_L drag-rise data-sets, and prediction of lift and moments were included in addition to the general focus on drag prediction.

The results of the first workshop[1] revealed relatively large scatter between submitted participant calculations using a wide range of codes. The results of the second workshop[3] demonstrated substantially reduced scatter, particularly for drag increment values between the two configurations, but still much higher levels than generally desirable. Furthermore, with several notable exceptions, the bulk of the computational results in both workshops demonstrated relatively poor agreement with experiment, especially in terms of lift versus incidence, and moment prediction. Several follow-on grid convergence studies with various structured and unstructured solvers[4–17] have also failed to resolve these discrepancies. These inconsistencies have been attributed, at least in part, to the existence of large pockets of separated flow on the DLR-F6 configuration. Although the configurations chosen for the two workshops consist of relatively simple geometries, the flow physics at the conditions of interest are more representative of off-design conditions due to the regions of separated flow. In a typical design study, once such regions of separated flow are discovered, the geometry would be modified until these regions are removed or at least minimized, producing a cleaner cruise configuration. A principal objective of the third and most recent workshop, DPW III, held in San Francisco, CA, in

*Professor, Department of Mechanical Engineering, University of Wyoming, AIAA Associate Fellow.

June 2006, was to test the hypothesis that the regions of separated flow were responsible for the wide scatter, poor grid convergence, and poor correlation with experimental data of the various Reynolds-averaged Navier-Stokes (RANS) codes. Additionally, the workshop sought to establish the performance of RANS codes both on clean attached flow cases, and on more difficult off-design cases with substantial amounts of separated flow.

For DPW III, a new wing-body fairing was designed[18] and added to the DLR-F6 wing body configuration in order to suppress flow separation in the wing-body juncture region. The baseline DLR-F6 wing-body configuration was also retained as a test case, providing a bridge between the two most recent workshops, and enabling the comparison of incremental values between clean and separated flow cases. Furthermore, in order to reduce the extent of the trailing edge separation observed on the baseline DLR-F6 configuration studied in DPW II, the Reynolds number for these cases was raised from 3 million to 5 million in DPW III. Because no experimental data currently exists at this Reynolds number for these two configurations (with and without fairing), DPW III constituted a "blind" CFD test case, and emphasis was placed on examining grid convergence and scatter between the various participating entries.

A wind tunnel test in the National Transonic Facility (NTF), at NASA Langley Research Center in Hampton VA, is planned for July 2007, which will be used to complement the numerical data-sets obtained through DPW III. The chosen Reynolds number of 5 million for DPW III corresponds to the highest estimated Reynolds number achievable in the NTF for this model running in air (non-cryogenically).

In addition to the two DLR-F6 wing-body configurations, a set of two wing-alone configurations were included as a second test case for DPW III. The purpose of this second test case was, on the one hand to provide a simpler wing-alone geometry, which would enable the use of higher grid resolution, thus enabling a more complete grid resolution study, and to provide a well behaved test case with no anticipated regions of separated flow. The use of two closely related wing geometries allowed for the assessment of predictions of increments in drag and other force and moment coefficients, as typically would be encountered in a design study.

The sequence of three workshops has enabled the assessment of the progress in the state-of-the-art of computational aerodynamics over the last half decade, made possible through advances in solver technology, grid generation capabilities, and computing hardware. As an example, the size of the grids used has grown substantially with each new workshop, particularly for the unstructured grid entries, with the largest unstructured grids in DPW I containing under 10 million points, and the largest unstructured grids in DPW III exceeding 40 million points.

The purpose of this paper is to document the results obtained in DPW III with the NSU3D unstructured mesh Reynolds averaged Navier-Stokes solver. The NSU3D solver has been a participant in all three workshops,[1,3,19] and has also been used in various follow-on studies, including comparison with other solvers,[2,8,9] sensitivity studies and extensive grid refinement studies[7,17]

I. Solver Description

The NSU3D code is an unstructured mesh multigrid Reynolds-averaged Navier-Stokes (RANS) solver for high-Reynolds number external aerodynamic applications. The NSU3D discretization employs a vertex-based approach, where the unknown fluid and turbulence variables are stored at the vertices of the mesh, and fluxes are computed on faces delimiting dual control volumes, with each dual face being associated with a mesh edge. This discretization operates on hybrid mixed-element meshes, generally employing prismatic elements in highly stretched boundary layer regions, and tetrahedral elements in isotropic regions of the mesh away from the aircraft surfaces. A single edge-based data-structure is used to compute flux balances across all types of elements. The convective terms are discretized as central differences with added matrix dissipation. Second-order accuracy is achieved by formulating these dissipative terms as an undivided biharmonic operator, which is constructed in two passes of a nearest-neighbor Laplacian operator. In the matrix form, this dissipation is similar to that produced by a Riemann solver gradient-based reconstruction scheme, and is obtained by replacing the difference in the reconstructed states on each side of the control volume interface by the undivided differences along mesh edges resulting from the biharmonic operator construction. These differences are then multiplied by the characteristic matrix to obtain the final dissipation terms.

The baseline NSU3D discretization employs a finite-difference scheme to approximate the thin-layer form of the viscous terms for the Navier-Stokes equations, although this is done in a multidimensional fashion, by computing a Laplacian of the velocity field.[20] The main approximation in this approach is the omission

of the cross-derivative viscous terms, and the assumption of a locally constant viscosity. The discretization of the full Navier-Stokes terms has also been implemented. This is achieved by first computing gradients of the flow variables at the grid vertices, using an edge-based loop, and then using a second edge loop to assemble the viscous flux balance at each vertex, based on these gradients. This approach results in an extended neighbor-of-neighbor stencil, which is less accurate than a nearest-neighbor stencil. However, a nearest-neighbor stencil discretization of second derivatives on mixed element meshes requires the use of a cell data-structure, while the current approach relies exclusively on the edge-data structure. In order to improve the accuracy and stability of this discretization, a hybrid approach is adopted, where the second derivatives in the directions aligned with the incident mesh edges are computed using a nearest-neighbor stencil on the edges, while the remaining terms are computed using the extended stencil using the two pass approach.

NSU3D incorporates the single equation Spalart-Allmaras turbulence model,[21] as well as a standard $k-\omega$ two-equation turbulence model.[22] All cases for DPW III were run using the Spalart-Allmaras turbulence model. Facilities for specified transition location based on the surface geometry are provided. While this capability was employed in DPW II,[3,9] the cases for DPW III were all run fully turbulent.

The basic time-stepping scheme in NSU3D consists of a three stage explicit multistage scheme. Convergence is accelerated by a local block-Jacobi preconditioner in regions of isotropic grid cells. In boundary layer regions, where the grid is highly stretched, a line preconditioner is employed to relieve the stiffness associated with the mesh anisotropy.[23] An agglomeration multigrid algorithm is used to further enhance convergence to steady-state.[20,24] The Jacobi and line preconditioners are used to drive the various levels of the multigrid sequence, resulting in a rapidly converging solution technique. Figure 1(a) illustrates a typical convergence history for the DLR-F6 wing-body with fairing configuration at Mach=0.75, 0 degrees incidence, and 5 million Reynolds number, using the 5.6 million, 14.6 million, and 41 million point grids supplied for DPW III, and described subsequently. The solver is generally run 500 multigrid cycles, and up to 1000 cycles for more stringent cases with larger amounts of separated flow. The convergence is seen to be similar for all three grids, with only slight decrease in the convergence rate as the grid resolution is increased. This is a property of the multigrid scheme, which is designed as an optimal solver to deliver convergence rates which are independent of the number of degrees of freedom.

On 16 AMD Opteron 242 processors, 500 multigrid cycles on the 5.0 million point grid requires approximately 4.0 hours of wall clock time. On 128 cpus of the NASA Columbia system (SGI Altix), this case requires 15 minutes of wall clock time. The availability of the NASA Columbia Supercomputer enables rapid turnaround for solutions on very fine grids. For example, on 128 cpus, a fine grid of 72 million points on the Wing-Body configuration required approximately 4.5 hours of cpu time to produce a converged solution. Figure 1(b) illustrates the scalability obtained on the NASA Columbia supercomputer for this 72 million point grid, going from 128 cpus to 2008 cpus, demonstrating slightly superlinear speedup. A computational rate of approximately 3 Tflops was obtained on 2008 cpus, using 5 multigrid levels. Using up to 6 multigrid levels reduces modestly the scalability and computational rates at high processor counts due to the increased amount of communication required on the coarse grid levels, but generally results in fastest overall convergence. On 2008 cpus, a solution on the 72 million point grid could be obtained in 20 minutes of wall clock time (2 seconds per multigrid cycle).

II. Preliminary Sensitivity Studies

Prior to DPW III, a sensitivity study of the NSU3D solver was carried out on the coarse, medium and fine grids supplied for the DLR-F6 wing-body case of the DPW II workshop.[17] Relevant findings from this study are included herein, in order to justify the choices made in running NSU3D for DPW III.

A. Thin Layer versus Full Navier-Stokes Terms

The flow field at the single condition of Mach=0.75 and 0 degrees incidence and Reynolds number of 3 million (DPW II value) has been computed on a family of progressively finer resolution grids (1M, 3M, 9M points) using the original multi-dimensional thin-layer approximation in the baseline NSU3D code, and also using the edge-based implementation of the full Navier-Stokes terms, as described previously. The computed values of the force coefficients are given in Table 1.

In all cases, the differences between the values computed with the thin-layer approximation and the

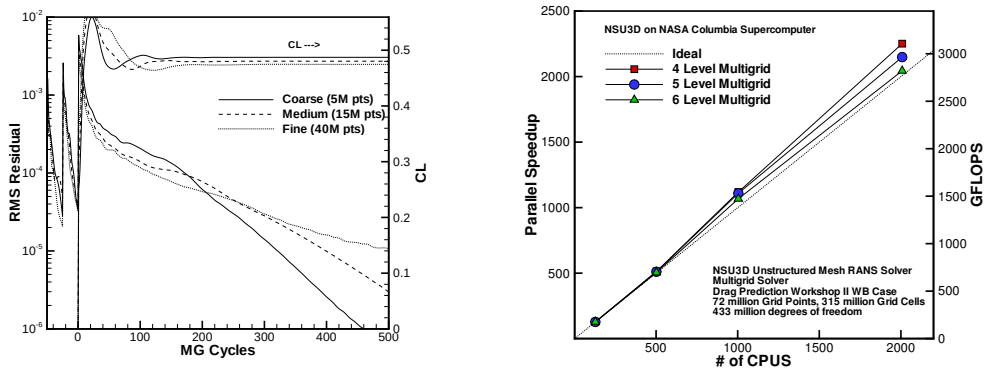

(a) (b)

Figure 1. (a): Multigrid convergence rate achieved on Wing-Body-Fairing Configuration at Mach=0.75, Reynolds = 5 million, and $\alpha = 0^o$ for coarse, medium and fine unstructured grids used in DPW III workshop. (b): Scalability and Computational Rates Achieved on NASA Columbia Supercomputer for NSU3D on a 72M point mesh for the Wing-Body test case illustrating the effect of various multigrid levels on overall scalability.

full Navier-Stokes terms are minimal, corresponding to less than 2 counts of drag for the finer meshes of the sequence, and small variations in the third significant figure of the lift coefficient. Note that for this case (DLR-F6 without fairing at 3 million Reynolds number), significant regions of flow separation are known to be present. However, based on the computed results, for these cases, the multi-dimensional thin-layer assumption appears to be justified, and little change in the solution is observed in going from the multi-dimensional thin layer to the full Navier-Stokes terms. All cases computed for DPW III described subsequently were run using the multi-dimensional thin-layer form of the viscous terms.

Table 1. Computed Lift and Drag Coefficients at Mach=0.75, Incidence=0^0, Reynolds number = 3 million, on various grids using the multi-dimensional thin-layer discretization and the extended stencil full Navier-Stokes discretization for Wing-Body configuration at Mach=0.75, $\alpha = 0.0^o$, Reynolds = 3 million.

Grid Size	Viscous Terms	C_L	C_D	$CD_{Pressure}$	$CD_{Friction}$
1M pts	Thin Layer Approx.	0.5055	0.02960	0.01661	0.01298
1M pts	Full Navier Stokes	0.4960	0.02921	0.01652	0.01269
3M pts	Thin Layer Approx.	0.5012	0.02859	0.01568	0.01290
3M pts	Full Navier Stokes	0.5020	0.02841	0.01571	0.01270
9M pts	Thin Layer Approx.	0.5141	0.02882	0.01592	0.01290
9M pts	Full Navier Stokes	0.5154	0.02867	0.01594	0.01273

B. Distance Function Sensitivity

The Spalart-Allmaras turbulence model requires knowledge of the distance to the nearest wall for each field grid point. This computation of this quantity has proved to be somewhat resource intensive, and also prone to error. In fact, small differences are known to exist between the results generated by various approaches to solving this problem on the same grid. The resulting distance function is not necessarily smooth, as the location of the closest surface can change discontinuously as one proceeds outwards in a concave region of the geometry, for example. This in turn implies that the accuracy of the computed distance may not scale with grid resolution in the same manner as the overall discretization error and may contribute to anomalies in a grid convergence study. To this effect, we study the sensitivity of the solution to various approaches for computing the distance function, including an exhaustive search procedure, generally acknowledged to produce the most "exact" values, but perhaps involving non-smooth variations in the distance function, and two partial-

differential-equation-based methods. The first approach involves the solution of the Eikonal equation,[25] while the second approach involves the solution of a Poisson equation.[26] While the first approach has been shown to produce distance function values which are more closely related to those produced by the exhaustive search method, the results are known to be only first-order accurate in space. The Poisson equation approach, on the other hand, produces distance values which deviate substantially from the exhaustive search values at large distances away from the wall, but are close to these values in near wall regions, and exhibit second-order discretization error. The Poisson equation approach is also the fastest distance function calculation method, since it can easily be parallelized and solved using the same multigrid approach used for the flow equations, while the Eikonal equation is solved with a sweeping approach, which is difficult to parallelize, and is currently implemented as a preprocessing step running on a single processor. Both these approaches are more than an order of magnitude faster than the exhaustive search method, and remain practical for very large mesh resolutions, where the cost of the exhaustive search approach becomes prohibitive.

The lift and drag values computed on the same 1M point, 3M point, and 9M point grids discussed above, using the three different distance function evaluation methods are given in Table 2, for the transonic flow conditions of Mach=0.75, 0^o incidence, and Reynolds number of 3 million. In all cases, the values obtained using the Eikonal equation approach are almost indistinguishable from those obtained with the exhaustive search method. For example, there is always substantially less than 1 count difference in the computed drag between these methods. The computed lift values are consistent to three significant figures, with the smaller differences observed on finer grids. The Poisson equation approach produces more discrepancies in the computed force coefficients, showing variations of 2.8 counts of drag and approximately 1% difference in the computed lift coefficient on the coarsest mesh, although these differences are reduced on the finer grid. Overall, the Eikonal equation approach is the preferred method, since it differs very little from the exhaustive search approach, but is over an order of magnitude faster in computing the distance function. On the other hand, this method is difficult to parallelize since it relies on a sweeping algorithm, and is currently implemented as a sequential preprocessing step.

The Eikonal equation approach has been used to calculate the distance function for all cases computed in DPW III, and described subsequently. On the finest grids considered, which contain slightly over 40 million points, the distance function computation using the Eikonal equation approach required approximately 45 minutes on a single Itanium processor of the NASA Columbia machine (SGI Altix system).

Table 2. Computed Lift and Drag Coefficients at Mach=0.75, Incidence=0^0, on various grids using three different approaches for computing the distance function.

Grid Size	Distance Function	C_L	C_D
1M pts	Exhaustive Search	0.50546	0.03139
1M pts	Eikonal Equation	0.50563	0.03138
1M pts	Poisson Equation	0.49915	0.03111
3M pts	Exhaustive Search	0.50732	0.02942
3M pts	Eikonal Equation	0.50751	0.02942
3M pts	Poisson Equation	0.50452	0.02927
9M pts	Exhaustive Search	0.51410	0.02882
9M pts	Eikonal Equation	0.51404	0.02882

III. DPW III: Case 1

A. Case 1 Description

The baseline DLR-F6 wing-body configuration has been previously described in the context of DPW II.[3] This is a generic wing-body configuration representative of modern supercritical wing transport aircraft design practices. The wing planform contains a trailing-edge break at the 41.1% span location, has a leading edge and quarter-chord sweep of 27.1^o and 25^o respectively, and an aspect ratio of 9.5. The original geometry has an acute angle of roughly 60^o between the fuselage and the wing upper surface, which results in flow separation at the wing-body juncture. A new wing-body fairing has been developed by Vassberg,[18] in order to suppress the side-of-body separation observed on the baseline wing-body geometry. The combination

of the original wing-body geometry with and without the newly designed fairing constitutes the set of two geometries studied in Case 1 for DPW III. Case 1 consists of a grid convergence study on the DLR-F6 wing-body with and without fairing, at a fixed $C_L = 0.5$ condition, at Mach = 0.75, and at the higher Reynolds number of 5 million (compared to 3 million used in DPW II). A drag polar (on the medium grid) was also required by varying the incidence ($\alpha = -3.0^o, -2.0^o, -1.0^o, -0.5^o, 0.0^o, 0.5^o, 1.0^o, 1.5^o$) while holding the Mach and Reynolds number conditions fixed at the above values.

B. Grid Generation

A total of six different grids were used for Case 1, consisting of a coarse, medium and fine grid for each configuration. These grids were generated at NASA Langley using the VGRID grid generation program,[27] and made available on the DPW III web site under the designation "LaRC Unstructured Node-Based".[28] The generated grids followed the gridding guidelines developed for the workshop, which are posted on the DPW web site,[28] and summarized in reference.[19] These guidelines include a farfield boundary at 100 chord lengths away, a normal spacing at the wall of $y^+ < 1.0$ for the coarsest grids, with progressively smaller spacings on the finer grids, chordwise spacings at the wing leading and trailing edges of approximately 0.1% chord on the coarse mesh, and spanwise spacings of 0.1% at the wing root and tip on the coarsest mesh as well. A resolution of 8, 12, and 16 cells across the blunt trailing edge of the wing was specified for the coarse, medium and fine grids respectively, and the overall size of the grids was targeted to grow by a factor of three when going from coarse to medium, and medium to fine. The medium grid was specified to be representative of the resolution level used in current industrial production runs.

An important consideration in a grid convergence study is to employ a sequence of grids using the same relative variations in spatial resolution and cell aspect-ratios throughout the domain, with global refinement or coarsening between the various grids of this so-called family.[29] In order to achieve a self-similar family of grids, a set of spacings was specified in the VGRID grid generation program using the source spacing method, and a global grid spacing rescaling was applied using the *ifact* global spacing factor in VGRID,[27] to obtain globally finer or coarser grids. Although this produces global variations in grid spacings, experimentation has shown that the desired changes in resolution are not always recovered exactly in all regions of the computational domain, although this is likely the best approximation to a self-similar family of grids that can be achieved using this methodology.[30]

Figure 2 illustrates the grid resolution in the critical wing-body juncture region for the wing-body-fairing geometry, for the coarse, medium and fine grids used in the NSU3D computations. The overall grid resolutions were substantially higher than those used in previous workshops, with the coarse grids containing approximately 5.6 million points, the medium grids 14.6 million points, and the fine grids exceeding 40 million points for both configurations. At this level, current industrial practice probably corresponds more closely to the coarse grid resolution rather than the medium grid resolution. The precise specifications for these grids are given in Table 3. All these grids were transformed into hybrid prismatic-tetrahedral grids by merging triplets of tetrahedra in the boundary layer regions into prismatic elements prior to the NSU3D computations.

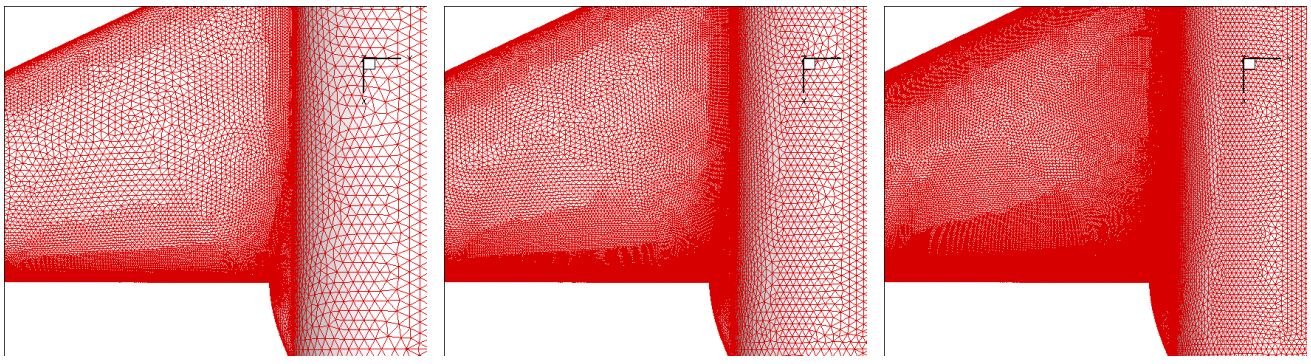

(a) (b) (c)

Figure 2. Wing-body-fairing grid resolution near wing-fuselage juncture for (a) coarse mesh (5.6 million points total), (b) medium mesh (14.6 million points total), and (c) fine mesh (41 million points total).

Table 3. Description of grids used for wing-body-fairing configuration. Global Spacing refers to the IFACT parameter which controls the global spacing for VGRID. Hybrid cell numbers are obtained through postprocessing of VGRID output.

	Wing-Body-Fairing			Wing-Body		
	Coarse	Medium	Fine	Coarse	Medium	Fine
Global Spacing	1.5	1.0	0.67	1.5	1.0	0.67
Boundary Pts	142,409	295,916	650,376	134,519	286,050	618,130
Total Grid Pts	5,618,073	14,598,610	41,069,036	5,354,214	14,298,135	40,014,934
Total Tetrahedra	33,037,458	85,850,911	241,486,342	31481575	84078830	235263704
Tetrahedra (Hybrid)	14,684,297	46,445,221	152,724,605	14,361,710	46,318,619	151,624,247
Prisms (Hybrid)	6,124,265	13,144,822	29,603,771	5,712,550	12,595,740	27,894,717
Pyramids (Hybrid)	38,738	57,007	98,737	34,940	53,443	88,448

C. NSU3D Results

In the absence of any experimental data, the numerical solutions were naturally concentrated on studying grid convergence. NSU3D was run on all three grids for each configuration at the fixed $C_L = 0.5$ condition. For the wing-body with fairing case, the complete incidence sweep was also run on all three grids. The convergence of NSU3D on all three grids at a fixed incidence of $\alpha = 0^o$ was previously discussed in Figure 1, showing only minor dependence on the grid resolution. In order to compute the fixed C_L condition, a C_L driver is required, which periodically adjusts the incidence value to maintain the required lift value throughout the convergence process. Figure 3(a) compares the convergence obtained for a fixed α versus a fixed C_L case, where the spikes in the residual plot correspond to step changes in α produced by the C_L driver. The constant lift case is initially run 200 multigrid cycles prior to engaging the C_L driver. At this point a step change in the incidence is generated which produces a spike in the residual convergence history. Subsequent incidence adjustments occur at regular intervals but become small enough to where their effect on the convergence history is no longer perceptible, and the overall fixed C_L convergence rate is equivalent to the fixed incidence convergence rate.

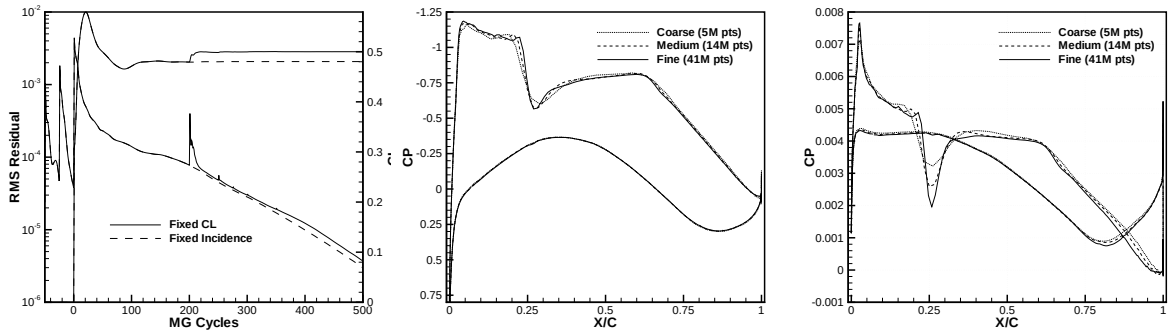

(a) (b) (c)

Figure 3. (a): Comparison of multigrid convergence for fixed incidence and fixed lift cases on medium grid (14.6M points) for wing-body-fairing geometry at Mach=0.75 and Reynolds = 5 million. (b): Comparison of computed surface pressure coefficients at 41.1% span location for coarse, medium and fine grids for wing-body-fairing geometry at Mach=0.75, Reynolds = 5 million, $C_L = 0.5$. (c): Comparison of computed skin-friction coefficients at same location and conditions on coarse, medium and fine wing-body-fairing grids.

In Figure 3(b), the computed surface pressure distributions are shown at the break section (41.1% span) for the three progressively finer grids, showing minimal effect of grid resolution on these values. This degree of sensitivity is typical for most solvers on most configurations in DPW III.[19] The computed surface skin-friction coefficients for the three different grid resolutions at the break section are shown in Figure 3(c),

Table 4. Location of trailing-edge separation as measured by $\frac{x}{chord}$ location of vanishing skin friction in direction normal to trailing-edge span line for coarse, medium, and fine grids for wing-body-fairing configuration at Mach=0.75, Reynolds= 5 million, and $C_L = 0.5$.

Station	Span ($\eta = \frac{y}{b}$)	x/c Coarse	x/c Medium	x/c Fine
1.	0.150	1.000	1.000	1.000
2.	0.239	0.991	0.982	0.981
3.	0.331	0.982	0.972	0.964
4.	0.377	0.978	0.973	0.975
5.	0.411	0.984	0.969	0.959
6.	0.514	0.971	0.957	0.947
7.	0.638	0.975	0.961	0.953
8.	0.847	0.983	0.969	0.954

showing similarly low sensitivity of these values to the grid resolution. The addition of the side-body fairing for this case was successful in completely eliminating the side-of-body flow separation which was observed both numerically and experimentally on the geometry with no fairing.[3,9,19] The fully attached nature of the flow is depicted in the plot of Figure 4(a), which shows the streamlines in the region of the wing-fuselage-fairing juncture. However, a region of separated flow remains in the vicinity of the trailing edge of the wing, as documented by the streamline traces in Figure 4(b), and in the trailing-edge separation points logged in Table 4, which are determined by the location where the skin-friction component in the direction normal to the trailing-edge span line become vanishes. In Table 4, separation is seen to occur in the vicinity of 95% to 98% chord, with increased separation regions occurring on progressively finer meshes. Figures 5(a) (b) and

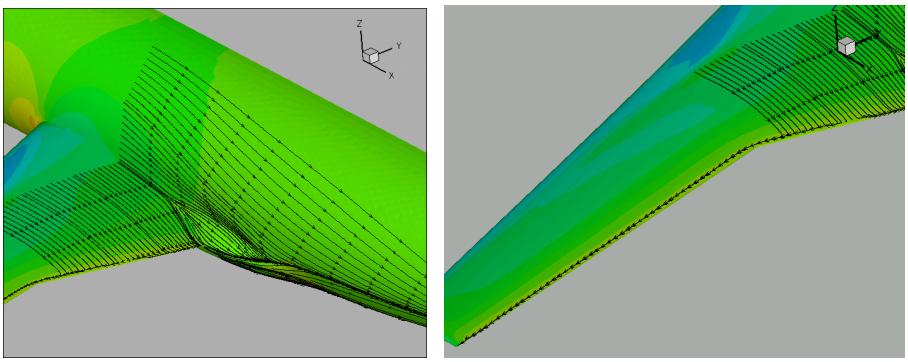

(a) (b)

Figure 4. (a): Surface streamline traces on coarse grid showing fully attached flow in wing-body juncture region for wing-body-fairing geometry at fixed $C_L = 0.5$ condition. (b): Surface streamline traces on coarse grid showing trailing-edge separation region for wing-body-fairing geometry at fixed $C_L = 0.5$ condition.

(c) depict the lift versus incidence, drag polar, and pitching moment as a function of lift computed on all three grids. Although the incidence sweep was only required on the medium grid, the use of all three grids permits the examination of the grid convergence effects over the complete incidence range. In general the trends are well behaved, with similar values and decreasing discrepancies when going to finer grids.

Figure 6(a) depicts the convergence history obtained on the medium grid for the Wing-Body case (without fairing) at a fixed incidence of $\alpha = 0^o$. In this case, the residual does not fully converge, but rather exhibits a periodic behavior, which is attributed to the periodic growing and shedding of the side-of-body separation region, as shown in the streamline traces of Figure 6(b). Figure 6(c) illustrates the extent of trailing-edge separation which is qualitatively similar to that observed on the wing-body-fairing configuration. The precise computed separation locations are documented in Table 5 for this case on the coarse, medium and fine grids. Convergence problems of this sort were experienced by various other entries in DPW III for this geometry.[19] In spite of the lack of residual convergence, variations in the final force coefficients remain relatively small, as can be seen from Figure 7(a), where the minimum and maximum values of the unsteady lift coefficient

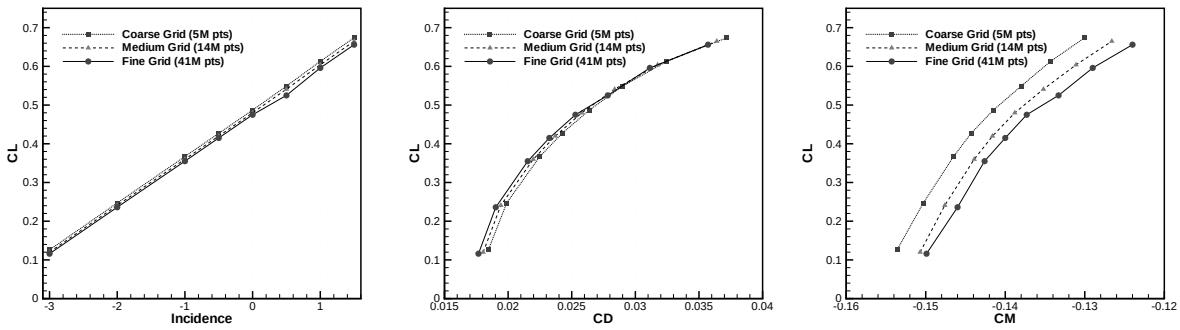

(a) (b) (c)

Figure 5. Computed values of (a) lift coefficient versus incidence, (b) drag polar and (c) pitching moment coefficient for complete range of incidences for wing-body-fairing geometry on coarse, medium and fine grids.

are plotted at each incidence. When plotted in drag polar form, these differences are even smaller, as seen in Figure 7(b) while they are somewhat larger when the pitching moment is considered, as shown in Figure 7(c). Nevertheless, it was felt that the computed average force coefficients were accurate enough to use in a grid convergence study and in examining increments between the wing-body-fairing and wing-body geometries.

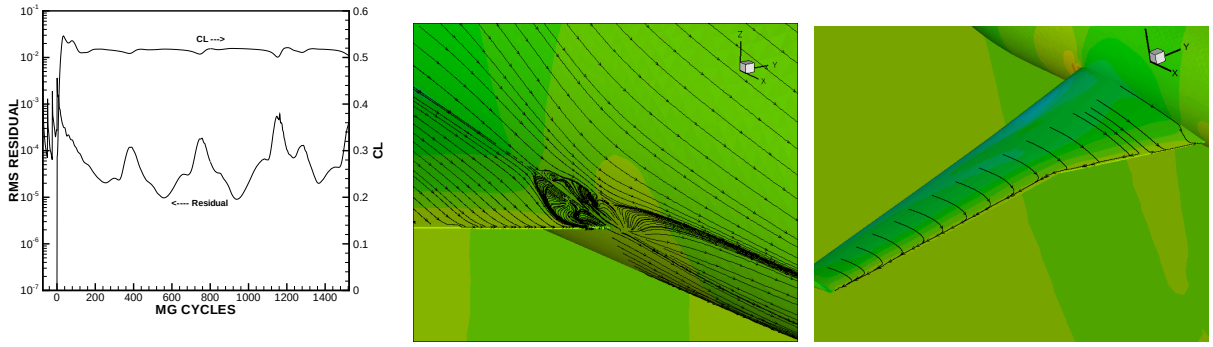

(a) (b) (c)

Figure 6. (a): Convergence rate on medium grid for wing-body configuration at Mach=0.75, Reynolds = 5 million, $\alpha = 0.0^o$ illustrating unsteady residual behavior. (b) Surface streamline traces on coarse grid showing separated flow in wing-body juncture region for wing-body geometry at fixed $C_L = 0.5$ condition. (c): Surface streamline traces on coarse grid showing trailing-edge separation region for wing-body geometry at fixed $C_L = 0.5$ condition.

Figures 8 and 9 compare the force and moment coefficients for the fixed $C_L = 0.5$ condition on the three grids for each geometry, as well as the incidence required to achieve this C_L condition. These values are plotted versus the inverse of the number of grid points to the $\frac{2}{3}$ power, with the understanding that, for a family of self-similar coarse to fine grids, this quantity should be representative of the average cell size h to the second power. Thus, straight-line plots in these figures are indicative of second-order accurate spatial convergence. The total drag convergence plots in Figure 8(a) produce a relatively straight line for the wing-body-fairing geometry, with a somewhat less well-behaved plot for the wing-body configuration. When these plots are broken down into pressure and friction drag, a slight compensating effect is observed for the wing-body-fairing case, although the deviation from straight-line behavior is not too severe as seen in Figures 8(b) and (c). On the other hand, the plots of the pitching moment coefficient and incidence values in Figures 9(a) and (b) result in relatively straight lines.

Table 5. Location of trailing-edge separation as measured by $\frac{x}{chord}$ location of vanishing skin friction in direction normal to trailing-edge span line for coarse, medium, and fine grids for wing-body configuration at Mach=0.75, Reynolds= 5 million, and $C_L = 0.5$.

Station	Span ($\eta = \frac{y}{b}$)	x/c Coarse	x/c Medium	x/c Fine
1.	0.150	1.000	1.000	1.000
2.	0.239	0.986	0.974	0.964
3.	0.331	0.987	0.971	0.963
4.	0.377	0.980	0.972	0.968
5.	0.411	0.974	0.970	0.959
6.	0.514	0.975	0.958	0.951
7.	0.638	0.978	0.961	0.952
8.	0.847	0.990	0.969	0.958

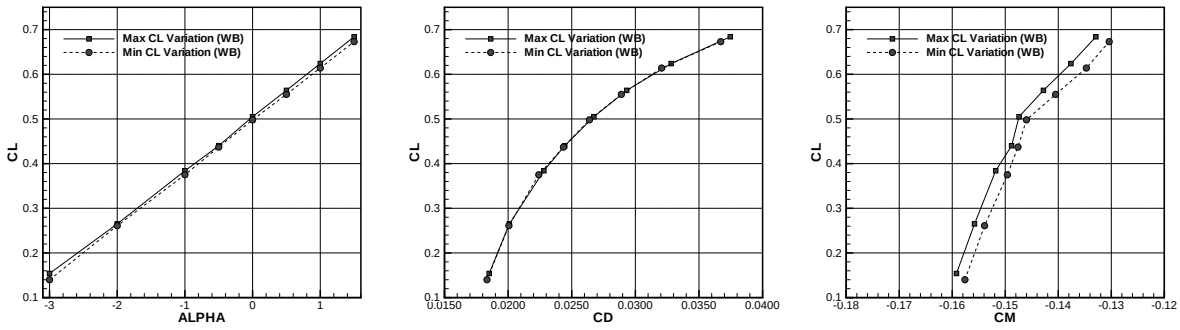

(a) (b) (c)

Figure 7. (a): Minimum and maximum values of unsteady lift coefficient computed at various incidences and (b) minimum and maximum values of unsteady lift and drag coefficients plotted in drag polar format and (c) minimum and maximum values of unsteady pitching moment versus lift coefficient on medium grid for wing-body configuration at Mach=0.75, Reynolds = 5 million.

In reference,[19] a figure of merit is defined for the various DPW III entries, which quantifies the deviation of these plots (broken down into pressure and friction drag) from straight-line behavior. The figure of merit computed for these NSU3D results is somewhat higher (i.e. worse) than 8 other entries, but remains the lowest of all the unstructured grid submissions. This is noteworthy, because the generation of a family of self-similar grids is much more speculative with unstructured grid methodologies, where the connectivity is not preserved and relative resolution variations may occur, compared to the generation of structured grid families. Figures 10 (a)(b)(c) provide a comparison of the wing-body with and without fairing on the medium grids, illustrating a consistent lift decrease at constant incidence due to the addition of the fairing, and a decrease in the pitching moment. The differences in drag when plotted in drag polar format are less substantial. Figure 9(c) depicts the computed drag increment between the two configurations at the constant $C_L = 0.5$ condition, for the three grid resolutions, where a value of 2 counts is reported on the medium and fine grids. By comparison, a total of 8 out of 13 workshop entries reported a drag increment between 0 and 5 counts at this condition, with 5 other entries reporting between 8 and 17 counts.[19]

In summary, the Case 1 results obtained using NSU3D indicate a reasonable level of grid convergence for both configurations, especially considering the difficulties associated with obtaining self-similar families of unstructured grids within a grid convergence study. On the other hand, the wing-body configuration does not exhibit full and robust convergence due to the side-of-body separation, as was noted by various other participants. This is partly in contrast with previous NSU3D results on this configuration from DPW II (at a Reynolds number of 3 million) and other grid refinement studies, where convergence even in the presence of this side-of-body separation was not an issue.[3,9,17] Additionally, results on this configuration (albeit at the lower Reynolds number of 3 million) using a very fine grid of 65 million points, but generated using different local resolution settings (and notably with substantially increased spanwise trailing-edge resolution) have been found in previous work to result in substantially different predictions, with lift decreases of the order of 10% at the same incidence as the current and previous results on other fine grids grids using up to 72 million points.[17] Therefore, the effect of local variations in grid resolution can be expected to have a strong influence on predictions particularly when substantial regions of separated flow are known to be present, and the measure of grid convergence based on a relatively limited family of coarse to fine grids may ultimately prove to be misleading.

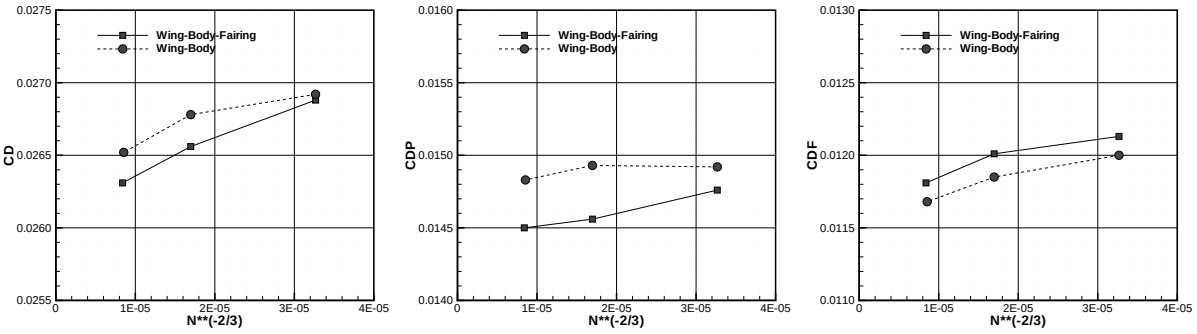

(a) (b) (c)

Figure 8. Grid convergence plots for (a) total drag, (b) pressure drag, (c) friction drag for wing-body-fairing and wing-body configurations at Mach=0.75, Reynolds = 5 million, $C_L = 0.5$ plotted as a function of the number of grid points to the $-\frac{2}{3}$ power.

IV. DPW III: Case 2

A. Case 2 Description

Case 2 is based on two generic wing-alone geometries designed by members of the DPW organizing committee. Both wings have a common trapezoidal planform shape with no leading or trailing-edge breaks. Leading edge and quarter chord sweep are 17.2^o and 15^o respectively. The airfoil sections selected for the first wing

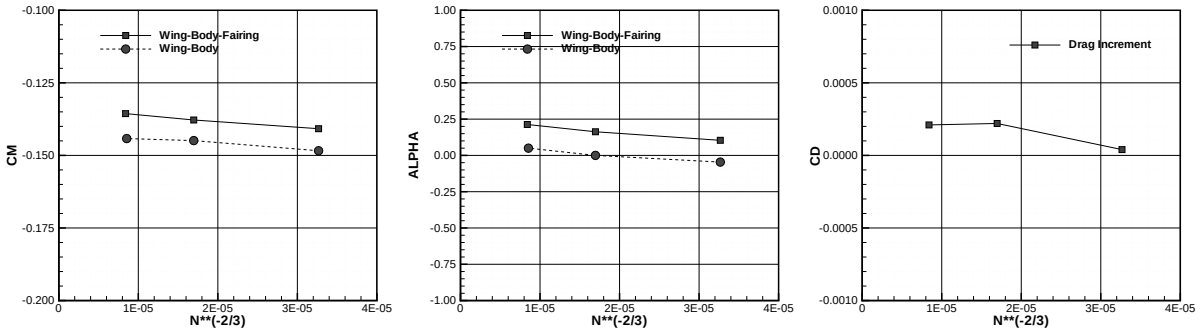

(a) (b) (c)

Figure 9. Grid convergence plots for (a) pitching moment, and (b) incidence, and (c) drag increment for wing-body-fairing and wing-body configurations at Mach=0.75, Reynolds = 5 million, $C_L = 0.5$ plotted as a function of the number of grid points to the $-\frac{2}{3}$ power.

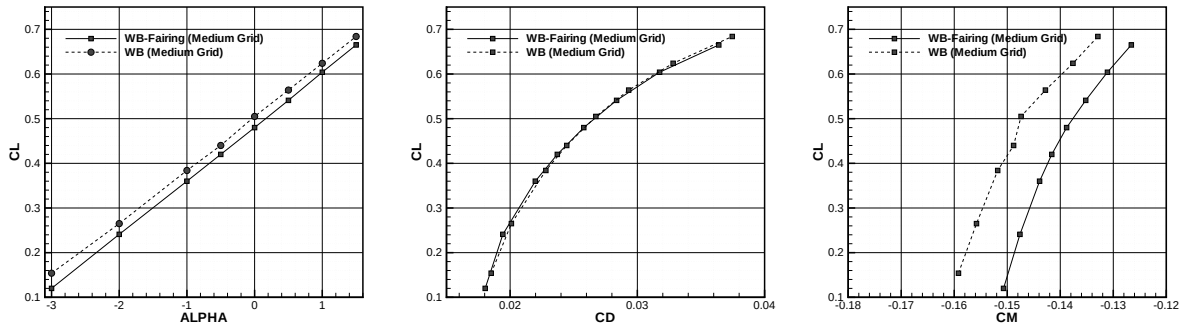

(a) (b) (c)

Figure 10. Comparison of (a) computed lift coefficient versus incidence, (b) drag polars, and (c) computed pitching moment coefficients for wing-body and wing-body-fairing cases on medium grid (15M points).

geometry (Wing1) are representative of supercritical sections found on modern transport aircraft, while the second wing geometry (Wing2) represents a slight modification of Wing1 obtained through a single-point optimization process. A more detailed description of these geometries can be found in references.[19,28]

The test case consists of a grid convergence study at fixed incidence of $\alpha = 0.5^o$ (as opposed to the fixed C_L condition of Case 1) at a Mach number of 0.76 and a Reynolds number of 5 million, in addition to a complete polar sweep for both geometries at incidences $\alpha = -1.0^o, 0.0^o, 0.5^o, 1.0^o, 1.5^o, 2.0^o, 2.5^o, 3.0^o$ on the medium grid. The relatively simple geometries of this test case enabled the use of a larger sequence of four rather than three coarse to fine grids, for a more complete grid convergence study. Additionally, the prediction of drag increments was targeted through the use of two closely related geometries.

B. Grid Generation

A total of eight different grids were used for Case II, consisting of a coarse, medium, fine, and extra-fine grid for each configuration. These grids were generated at NASA Langley using the VGRID grid generation program,[27] and made available on the DPW III web site under the designation "LaRC Unstructured Node-Based".[28] The generated grids followed the same gridding guidelines developed for the workshop mentioned previously, and summarized in References.[19,28] The same approach was used within the VGRID program for producing a family of self-similar coarse to fine meshes. The grid sizes range from 1.8 million points for the coarse mesh, to 39 million points for the extra-fine mesh, with the principal grid characteristics detailed in Table 6.

In addition to the cases run at the University of Wyoming, NSU3D was also used to compute Case 2 at Cessna Aircraft Co. using a different set of grids generated independently, but in the same fashion with VGRID. These grids, which are somewhat coarser than the NASA Langley VGRID submissions of Table 6, are described in Table 7. These grids are also available on the DPW web site under the designation "Cessna Unstructured". All these grids were transformed into hybrid prismatic-tetrahedral grids by merging triplets of tetrahedra in the boundary layer regions into prismatic elements prior to the NSU3D computations.

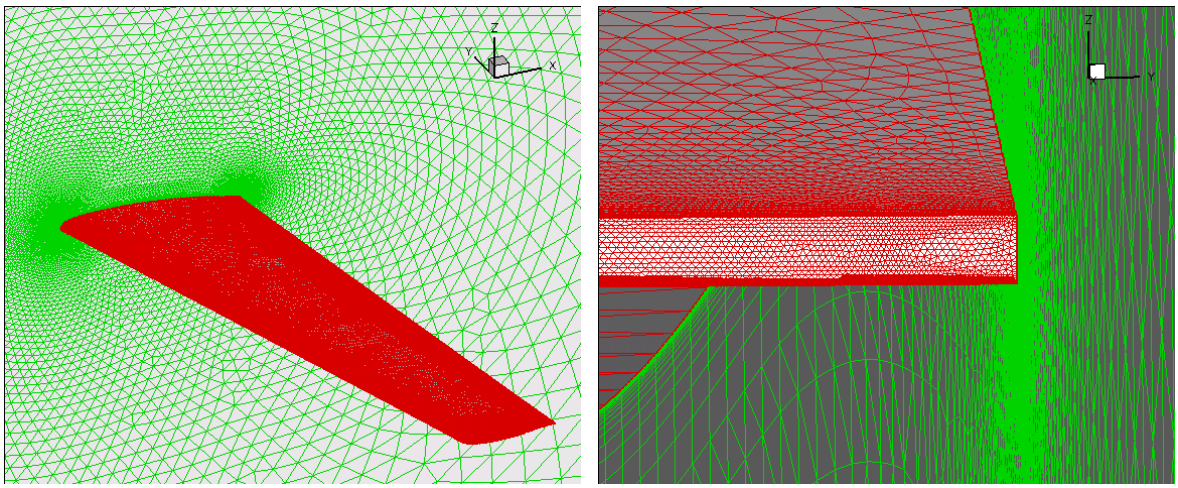

(a) (b)

Figure 11. (a): Fine Grid on Wing1 Configuration comprising a total of 15 million points. (b): Detail of trailing-edge base resolution for fine grid on Wing1 Configuration containing approximately 16 cells across blunt trailing-edge base.

C. NSU3D Results

The convergence of NSU3D on the four meshes of the Wing2 configuration described in Table 6 is depicted in Figure 12(a). The convergence degrades on the fine and extra-fine grid, but this is attributed to unsteadiness in the small regions of separated flow at the blunt trailing edge, and has little effect on the overall force coefficient convergence. On all grids, the force coefficients are well converged (to 4 significant figures) within 500 multigrid cycles. Run times are similar to those described in Case 1, ranging from 1 hour on a cluster

Table 6. Description of grids used for Wing1 and Wing2 at University of Wyoming. Global spacing refers to the IFACT parameter which controls the global spacing for VGRID. Hybrid cell numbers obtained through postprocessing of VGRID output.

	Wing1				Wing2			
	Coarse	Medium	Fine	Extra-Fine	Coarse	Medium	Fine	Extra-Fine
Global Spacing	1.5	1.0	0.67	0.44	1.5	1.0	0.67	0.44
Boundary Pts	52,243	110,866	235,347	611,352	54,436	115,537	245,871	646,905
Total Grid Pts	1,806,422	4,476,969	11,459,041	36,900,028	1,882,672	4,658,853	11,903,329	38,462,630
Total Tetrahedra	10,639,646	26,368,110	67,463,143	217,160,940	11,088,290	27,437,220	70,081,360	226,386,508
Tetrahedra (Hybrid)	3,468,031	10,776,742	33,986,137	129,263,675	3,505,367	11,031,889	34,643,714	131,845,381
Prisms (Hybrid)	2,394,517	5,203,102	11,170,104	29,317,606	2,531,620	5,475,195	11,822,866	31,531,608
Pyramids (Hybrid)	24,247	36,401	67,307	112,201	22,864	39,178	60,294	105,474

Table 7. Description of grids used for Wing1 and Wing2 at Cessna Aircraft Co. Global spacing refers to the IFACT parameter which controls the global spacing for VGRID. Hybrid cell numbers obtained through postprocessing of VGRID output.

	Wing1				Wing2			
	Coarse	Medium	Fine	Extra-Fine	Coarse	Medium	Fine	Extra-Fine
Global Spacing	1.5	1.0	0.67	0.5	1.5	1.0	0.67	0.5
Boundary Pts	35,270	70,449	139,768	236,291	33,993	67,138	134,164	227,109
Total Grid Pts	983,633	2,417,082	6,138,245	12,748,678	947,409	2,325,884	5,963,713	12,419,567
Total Tetrahedra	5,764,887	14,183,211	36,042,265	74,879,730	5,551,476	1,3647,064	35,016,693	72,945,687
Tetrahedra (Hybrid)	2,092,537	6,489,449	20,333,823	47,517,513	2,044,892	6,354,212	19,963,420	46,681,598
Prisms (Hybrid)	1,225,849	2,567,458	5,240,975	9,127,643	1,170,419	2,433,528	5,022,264	8,761,108
Pyramids (Hybrid)	10,249	16,909	28,601	41,131	9,366	15,559	27,083	38,625

of 16 Opterons for the coarsest grid, to 3 hours using 96 cpus on the NASA Columbia machine for the finest grid. The streamline traces for Wing2 in Figure 16(b) show fully attached flow over the wing, with incipient separation at the trailing edge. Examination of the surface skin-friction values indicates fully attached flow except on the extra-fine mesh where separation around 99.9% chord was observed.

The drag polar calculation was computed using the fine grid for both configurations (15M points), rather than the medium grid, as specified in the DPW III guidelines. Figures 13 illustrate the results of this exercise, comparing the values of lift, drag, and moment for both configurations throughout the range of incidences. The trends are generally consistent with those reported by other workshop participants. The Wing2 configuration, which is a single-point optimization of Wing1, produces slightly higher lift at $\alpha = 0.5^o$ (recall that the optimization was performed at constant lift), although these trends become reversed at higher incidences. The magnitude of the pitching moment for Wing2 is also substantially reduced compared to Wing1 over a broad range of incidences. Figures 14(a) and (b) depict the computed surface pressure

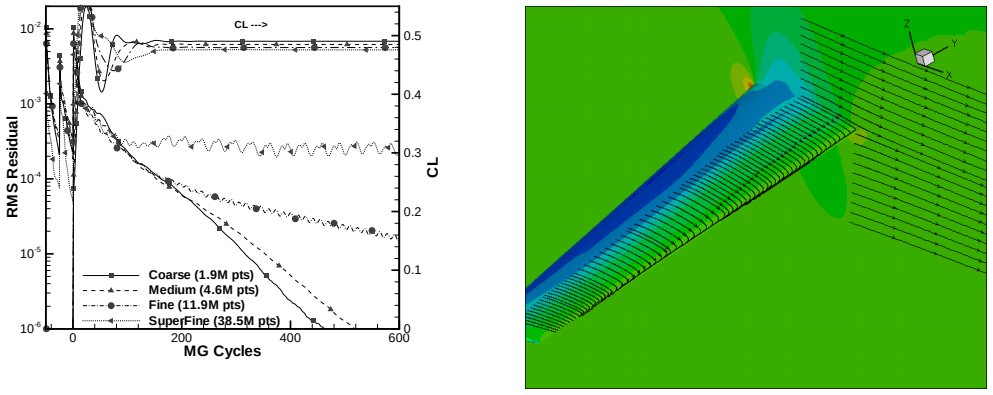

(a) (b)

Figure 12. Multigrid convergence histories for sequence of four grids for Wing2 configuration and (b) Surface streamline traces for Wing2 configuration on coarse grid at Mach = 0.76, $\alpha = 0.5^o$, and Reynolds = 5 million.

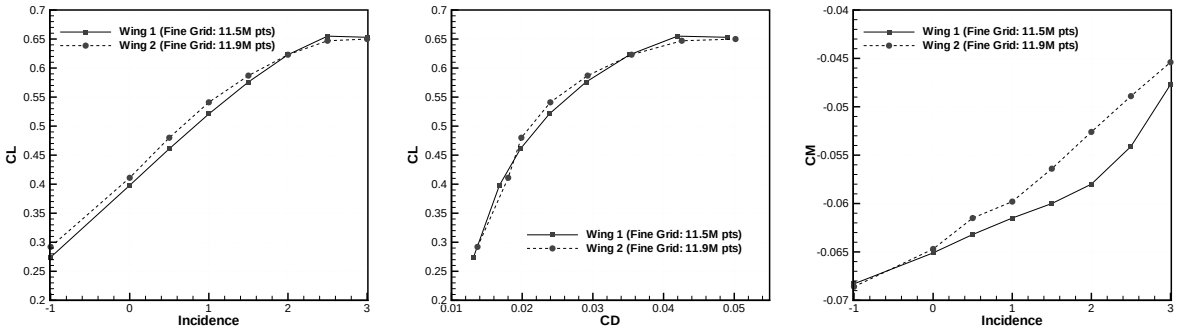

(a) (b) (c)

Figure 13. Comparison of (a) computed lift coefficient versus incidence, (b) drag polars, and (c) computed pitching moment coefficients for Wing1 and Wing2 on medium grid (15M points).

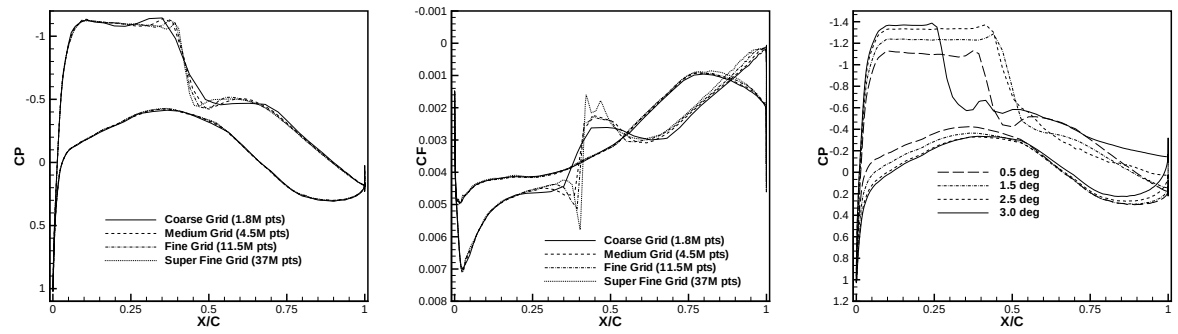

(a) (b) (c)

Figure 14. (a) Computed surface pressure coefficients and (b) skin-friction coefficients at the 55.1% span location at Mach = 0.76, $\alpha = 0.5^o$, Reynolds = 5 million, on the four grids used in the grid refinement study for Wing1. (c) Surface pressure coefficients at same location on medium grid for Wing1 at various incidences illustrating forward movement of shock at high incidences.

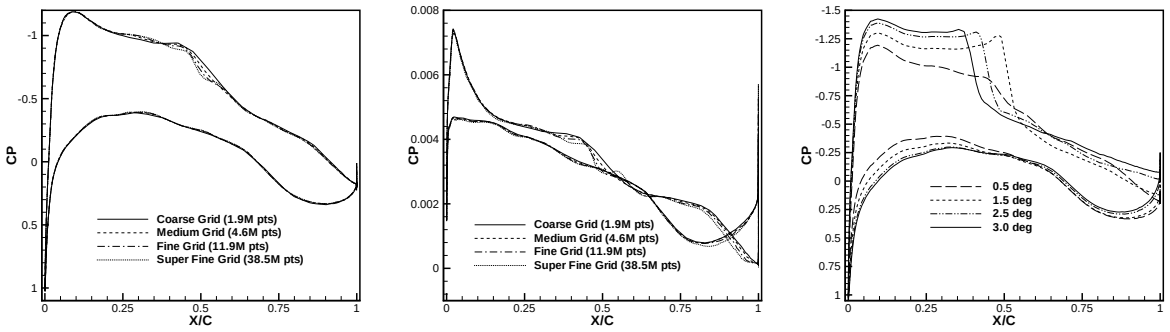

(a) (b) (c)

Figure 15. (a) Computed surface pressure coefficients and (b) skin-friction coefficients at the 55.1% span location at Mach = 0.76, $\alpha = 0.5^o$, Reynolds = 5 million, on the four grids used in the grid refinement study for Wing2. (c) Surface pressure coefficients at same location on medium grid for Wing2 at various incidences illustrating forward movement of shock at high incidences.

coefficients and skin-friction coefficients at the 55.1% span location for the various grids of the sequence for Wing1, with the only notable differences in going from coarse to fine grids in the resolution of the shock wave. Figure 14 (c) illustrates the computed surface pressure coefficients at the same span location on the fine grid (15M points) for various incidences used in the drag polar calculation. Note that the shock has moved forward and the wing is stalled at the highest incidence of 3.0^o. Equivalent results are presented for Wing2 in Figures 15 (a)(b)(c), showing similar trends. The notable difference is the weakness of the shock for the optimized wing at $\alpha = 0.5^o$, which is close to the single design point for Wing2 (which was optimized at constant C_L).

Figures 16 depict the grid convergence results for both configurations on the four-grid sequence of Table 6, which were run at the University of Wyoming, and on the grid sequence of Table 7, which were run at Cessna Aircraft Co. Concentrating initially on the first set of grids (Table 6), straight-line behavior indicative of second-order accurate spatial convergence is observed for virtually all quantities, including drag quantities broken down into pressure and friction values, and the drag increment computed between the two configurations. The quality of this grid convergence is distinctly superior to that obtained for the wing-body configurations in Case 1, and the addition of a fourth grid provides an even more convincing data-set. In fact, these results displayed the most consistent second-order accurate behavior out of all reported results for Case 2 in DPW III, as determined by the figure-of-merit calculation performed in reference.[19]

On the other hand, the results obtained using the second set of grids (c.f. Table 7) are somewhat at odds with the former results. The plots corresponding to this latter set of grids does not collapse as neatly to a straight line behavior, although the overall deviation is still not too substantial (ranked third by figure-of-merit method in reference[19]). This could possibly be attributed to a less than perfect self-similarity between the various grids of this family. Perhaps more concerning, however, is the fact that the two families of grids do not appear to be converging to the same continuum values in the limit of infinite mesh resolution. Some of these differences have been attributed to a reduced chordwise resolution of the second family of grids (c.f. Table 7), which produces a less well resolved shock and generally higher lift and lower pitching moment values, as seen in Figures 17(a) and (b). The drag increment computed on the two different grid families displays similar behavior as seen in Figure 18(a). On the other hand, the idealized drag, defined as $C_{D_{IDEAL}} = C_D - {C_L}^2/(\pi AR)$ where AR denotes the planform aspect ratio, shows consistent drag convergence on both families of grids, as seen in Figure 18(b). This implies that the differences in drag prediction between the two families of grids are due to the induced drag associated with different lift predictions. Although this validates the approach taken in Case 1 of performing the grid resolution study at constant C_L, mathematically one should still expect grid convergence of all solution values (i.e. lift and drag) for sufficiently fine grids, and the current results once again illustrate the difficulty in ascertaining grid convergence across different families of grids, particularly for problems such as computational aerodynamics, where the range of scales and thus grid resolution must necessarily vary many orders of magnitude. This

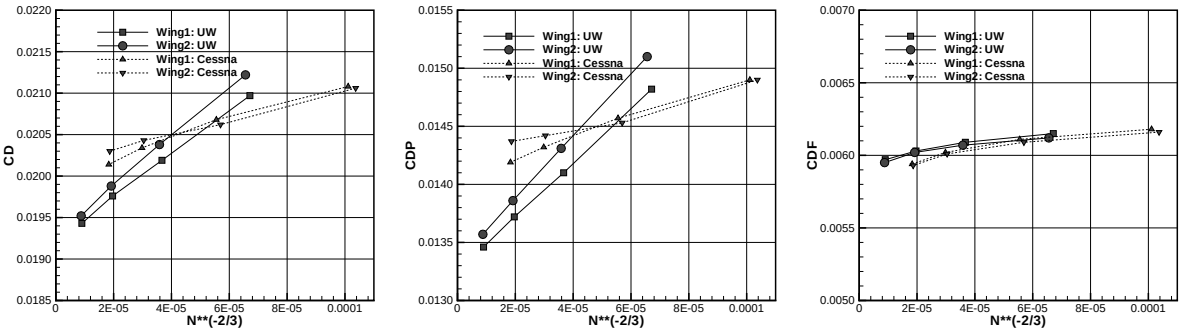

(a) (b) (c)

Figure 16. Grid convergence plots for (a) total drag, (b) pressure drag, (c) friction drag for Wing1 and Wing2 configurations at Mach=0.76, Reynolds = 5 million, $\alpha = 0.5^o$ plotted as a function of the number of grid points to the $-\frac{2}{3}$ power for two families of grids.

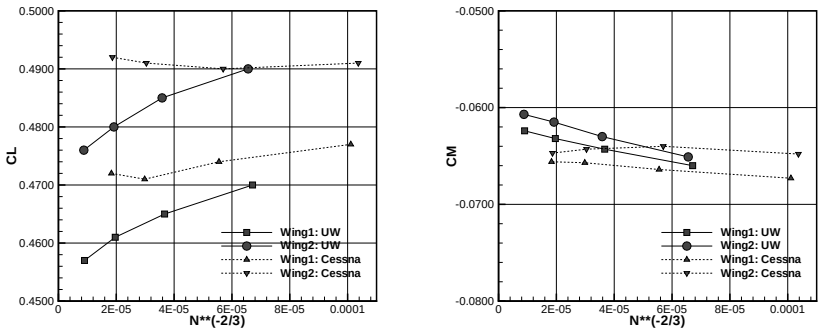

(a) (b)

Figure 17. Grid convergence plots for (a) lift coefficient, and (b) pitching moment for Wing1 and Wing2 configurations at Mach=0.76, Reynolds = 5 million, $\alpha = 0.5^o$ plotted as a function of the number of grid points to the $-\frac{2}{3}$ power for two families of grids.

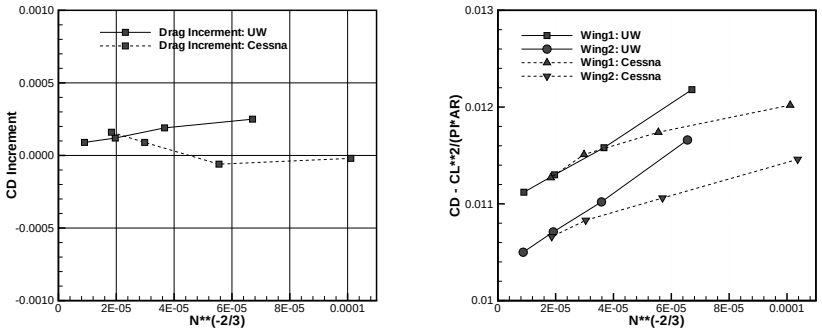

(a) (b)

Figure 18. Grid convergence plots for (a) drag increment, and (b) idealized drag, for Wing1 and Wing2 configurations at Mach=0.76, Reynolds = 5 million, $\alpha = 0.5^o$ plotted as a function of the number of grid points to the $-\frac{2}{3}$ power for two families of grids.

makes it unfeasible to fully resolve all regions through successive global mesh refinements without a good initial guess at the required local mesh resolutions, thus resulting in some dependence on the initial mesh configuration or the definition of the family of meshes.

V. Conclusion

Results from the third AIAA Drag prediction workshop using NSU3D have demonstrated solution accuracy and efficiency equivalent to other state-of-the-art structured, overset, and unstructured RANS solvers. Although changes in grid resolution have an almost trivial effect on computed surface distributions such as surface pressures and skin-friction coefficients, the overall effect on integrated quantities such as lift, drag and pitching moment can be substantial, especially considering the accuracy requirement of aerodynamic design studies (i.e. drag to 1 count accuracy). The NSU3D results from DPW3 displayed consistent second-order accurate grid convergence compared to other DPW3 entries, especially given the uncertainties inherent in generating families of self-similar unstructured grids. However, in Case 2 of this workshop, as well as in previous grid refinement studies,[17] different grid converged results may be predicted using different families of grids. The range of scales inherent in computational aerodynamics problems, which may easily vary by over six orders of magnitude, make it unfeasible to fully resolve all regions of the computational domain through successive global refinements of an arbitrarily constructed initial grid, resulting in a dependence on the initial grid and resulting families of grids obtained by successive refinements. An obvious remedy may include the use of adaptive meshing, although the success of this approach rests on the ability to formulate adequate and robust refinement criteria. In this respect, adjoint-based error-estimation techniques offer some promise,[31] although caveats remain, particularly considering the fact that these methods are based on a linearization of what may be an extremely non-linear problem.

Finally, the third drag prediction workshop provides an objective assessment of the state-of-the-art of computational aerodynamics. On the one hand, our capabilities for generating and computing on ever increasing grid sizes with faster turnaround times producing more accurate solutions with less scatter is increasing continuously, while on the other hand, a complete understanding and quantification of the various sources of errors including discretization, algebraic, and modeling errors is still in its infancy.

VI. Acknowledgements

Special thanks are due to E.M. Lee-Rausch of NASA Langley Research center for generating and providing the high-resolution and high quality "LaRC Unstructured Node-Based" grids for the workshop which were used in this work. Special thanks are also due to Tom Zickuhr of Cessna Aircraft Co. for providing the additional NSU3D results for Case 2. This work was also partly enabled thanks to computer time provided

on the NASA Columbia Supercomputer at the NASA Advanced Supercomputing Division (NAS).

References

[1]Levy, D. W., Zickuhr, T., Vassberg, J., Agrawal, S., Wahls, R. A., Pirzadeh, S., and Hemsch, M. J., "Summary of Data from the First AIAA CFD Drag Prediction Workshop," AIAA Paper 2002-0841.

[2]Mavriplis, D. J. and Levy, D. W., "Transonic Drag Prediction using an Unstructured Multigrid Solver," *AIAA Journal of Aircraft*, Vol. 42, No. 4, 2003, pp. 887–893.

[3]Laflin, K., Brodersen, O., Rakowitz, M., Vassberg, J., Wahls, R., and Morrison, J., "Summary of Data from the Second AIAA CFD Drag Prediction Workshop," AIAA Paper 2004-0555.

[4]Rakowitz, M., Eisfeld, B., Schwamborn, D., and Sutcliffe, M., "Structured and Unstructured computations on the DLR-F4 wing-body configuration," *AIAA Journal of Aircraft*, Vol. 40, No. 2, 2003, pp. 256–264.

[5]Pirzadeh, S. Z. and Frink, N. T., "Assessment of the Unstructured Grid Software TetrUSS for Drag Prediction of the DLR-F4 Configuration," AIAA Paper 2002-0839.

[6]Vassberg, J. C., Buning, P. G., and Rumsey, C. L., "Drag Prediction for the DLR-F4 Wing/Body using OVERFLOW and CFL3D on an Overset Mesh," AIAA Paper 2002-0840.

[7]Mavriplis, D. J., "Aerodynamic Drag Prediction Using Unstructured Mesh Solvers," *CFD-Based Drag Prediction and Reduction, eds. H. Deconoinck, K. Sermus and C. van Dam, VKI Lecture Series 2003-02, von Karman Institute for Fluid Dynamics, Rhode St-Genese, Belgium*, March 2003.

[8]Lee-Rausch, E. M., Buning, P. B., Mavriplis, D. J., Morrison, J. H., Park, M. A., Rivers, S. M., and Rumsey, C. L., "CFD Sensitivity Analysis of a Drag Prediction Workshop Wing/Body Transport Configuration," AIAA Paper 2003-3400.

[9]Lee-Rausch, E. M., Frink, N. T., Mavriplis, D. J., Rausch, R. D., and Milholen, W. E., "Transonic Drag Prediction on a DLR-F6 Transport Configuration using Unstructured Grid Solvers," AIAA Paper 2004-0554.

[10]Brodersen, O. P., Rakowitz, M., Amant, S., Larrieu, P., Destarac, D., and Suttcliffe, M., "Airbus, ONERA and DLR Results from the Second AIAA Drag Prediction Workshop," *AIAA Journal of Aircraft*, Vol. 42, No. 4, 2005, pp. 932–940.

[11]Langtry, R. B., Kuntz, M., and Menter, F., "Drag Prediction of Engine-Airframe Interference Effects with CFX-5," *AIAA Journal of Aircraft*, Vol. 42, No. 6, 2005, pp. 1523–1529.

[12]Sclafani, A., DeHaan, M., and Vassberg, J. C., "OVERFLOW Drag Prediction for the DLR-F6 Transport Configuration: A DPW-II Case Study," AIAA Paper 2004-0393.

[13]Rumsey, C., Rivers, S., and Morrison, J., "Study of CFD Variation on Transport Configurations from the Second Drag-Prediction Workshop," AIAA Paper 2004-0394.

[14]Yamamoto, K., Ochi, A., Shima, E., and Takaki, R., "CFD Sensitivity of Drag Prediction on DLR-F6 Configuration by Structured Method and Unstructured Method," AIAA Paper 2004-0398.

[15]Tinoco, E. and Su, T., "Drag Prediction with the Zeus/CFL3D System," AIAA Paper 2004-0552.

[16]Klausmeyer, S., "Drag, Lift, and Moment Estimates of Transonic Aircraft Using the Navier-Stokes Equations," AIAA Paper 2004-0553.

[17]Mavriplis, D. J., "Grid Resolution Study of a Drag Prediction Workshop Configuration Using the NSU3D Unstructured Mesh Solver," AIAA-Paper 2005-4729.

[18]Vassberg, J. C., Sclafani, A., and DeHaan, M., "A Wing-Body Fairing Design for the DLR-F6 Model: A DPW-III Case Study," AIAA Paper 2005-4730.

[19]Vassberg, J. C., Tinoco, E. N., Mani, M., Brodersen, O. P., Eisfeld, B., Wahls, R. A., Morrison, J. H., Zickuhr, T., Laflin, K. R., and Mavriplis, D. J., "Summary of the Third AIAA CFD Drag Prediction Workshop," AIAA Paper 2007-0260.

[20]Mavriplis, D. J. and Venkatakrishnan, V., "A Unified Multigrid Solver for the Navier-Stokes Equations on Mixed Element Meshes," *International Journal for Computational Fluid Dynamics*, Vol. 8, 1997, pp. 247–263.

[21]Spalart, P. R. and Allmaras, S. R., "A One-equation Turbulence Model for Aerodynamic Flows," *La Recherche Aérospatiale*, Vol. 1, 1994, pp. 5–21.

[22]Wilcox, D. C., "Re-assessment of the scale-determining equation for advanced turbulence models," *AIAA Journal*, Vol. 26, 1988, pp. 1414–1421.

[23]Mavriplis, D. J., "Multigrid Strategies for Viscous Flow Solvers on Anisotropic Unstructured Meshes," *Journal of Computational Physics*, Vol. 145, No. 1, Sept. 1998, pp. 141–165.

[24]Mavriplis, D. J. and Pirzadeh, S., "Large-Scale Parallel Unstructured Mesh Computations for 3D High-Lift Analysis," *AIAA Journal of Aircraft*, Vol. 36, No. 6, Dec. 1999, pp. 987–998.

[25]Sethian, J. and Vladimirsky, A., "Fast methods for the Eikonal and related Hamilton- Jacobi equations on unstructured meshes," *Applied Mathematics*, Vol. 97, No. 11, 2000, pp. 5699–5703.

[26]Tucker, P. G., Rumsey, C. L., Spalart, P. R., Bartels, R. E., and Biedron, R. T., "Computations of Wall Distances Based on Differential Equations," *AIAA Journal*, Vol. 43, No. 3, 2005, pp. 539–549.

[27]Pirzadeh, S., "Three-Dimensional Unstructured Viscous Grids by the Advancing-Layers Method," *AIAA Journal*, Vol. 34, No. 1, 1996, pp. 43–49.

[28]"Third AIAA Drag Prediction Workshop. San Francisco, CA," http://aaac.larc.nasa.gov/tsab/cfdlarc/aiaa-dpw.

[29]Salas, M. D., "Some Observations on Grid Convergence," *Journal of Computational Science*, Vol. 35, 2006, pp. 688–692.

[30]Lee-Rausch, E. M., "Private Communication," .

[31]Lee-Rausch, E. M., Park, M., Nielsen, E., Jones, W., and Hammond, D., "Parallel Adjoint-Based Error Estimation and Anisotropic Grid Adaptation for Three-Dimensional Aerospace Applications," AIAA Paper 2005-4842.